Quantum-enhanced ladar ranging with squeezed-vacuum injection, phase-sensitive amplification, and slow photodetectors

Invited Paper

Quantum-enhanced ladar ranging with squeezed-vacuum injection, phase-sensitive amplification, and slow photodetectors

Ranjith Nair[a], Brent J. Yen[a], and Jeffrey H. Shapiro[a]; Jian Chen[b], Zachary Dutton[b], Saikat Guha[b], and Marcus P. da Silva[b]

[a]Research Laboratory of Electronics, Massachusetts Institute of Technology, Cambridge, MA 02139, USA
[b]Raytheon BBN Technologies, 10 Moulton St, Cambridge, MA 02138, USA

ABSTRACT

Theory has shown [1] that the quantum enhancements afforded by squeezed-vacuum injection (SVI) and phase-sensitive amplification (PSA) can improve the spatial resolution of a soft-aperture, homodyne-detection laser-radar (ladar) system. Here we show they can improve the range resolution of such a ladar system. In particular, because an experimental PSA-enhanced system is being built whose slow photodetectors imply multi-pulse integration, we develop range-measurement theory that encompasses its processing architecture. We allow the target to have an arbitrary mixture of specular and speckle components, and present computer simulation results demonstrating the range-resolution improvement that accrues from quantum enhancement with PSA.

Keywords: Ladar, Ranging, Homodyne Detection, Squeezing, Phase-sensitive amplification

1. INTRODUCTION

It was shown in [1] that a coherent ladar that employs phase-sensitive amplification prior to homodyne detection has superior transverse spatial resolution compared to one that does not. For the case of a receiver input aperture with a soft rolloff in transmission (that may be desirable for apodizing the point-spread function of an original hard aperture), it was also shown that the injection of squeezed-vacuum light at the soft aperture also led to improved spatial resolution. These conclusions were subsequently found to hold even when the amplification and squeezing parameters of the various input and injection field modes are non-uniform, and hence more faithful to the situation in a real experiment [2]. In this paper, we show—through theory and simulation—that the use of phase-sensitive amplification and/or squeezed-vacuum injection in a homodyne ladar receiver also improve the longitudinal (range) resolution on a distant target by reducing the variance of the maximum-likelihood range estimator. We do this both for specular and speckle point targets, and we allow for detectors whose integration time is much longer than the temporal duration of the range-delay resolution bins.

In Sect. 2, we describe the coherent ladar system under study in general terms, including the ranging system architecture. In Sect. 3, we derive formulas for the homodyne-measurement statistics using the fully-quantum treatment necessary for describing a system that incorporates both squeezed-vacuum injection (SVI) and phase-sensitive amplification (PSA). The special cases of PSA-only and the semiclassical baseline incorporating no quantum enhancement whatsoever are emphasized. Our treatment applies both to specular point targets and mixed targets with both specular and speckle reflectivity components. In Sect. 4, the maximum-likelihood (ML) range estimator is derived, and simulation results are presented that predict quantum enhancements in range-estimate variance for both specular and speckle targets.

2. QUANTUM-ENHANCED COHERENT LADAR: SYSTEM DESCRIPTION

Here we will describe the quantum-enhanced homodyne ladar system. In Subsect. 2.1, we obtain the form of the homodyne-photocount operator, and in Subsect. 2.2, we obtain the operator description of our ladar system enhanced with squeezed-vacuum injection and phase-sensitive amplification.

Quantum Communications and Quantum Imaging IX, edited by
Ronald E. Meyers, Yanhua Shih, Keith S. Deacon, Proc. of SPIE Vol. 8163,
816310 · © 2011 SPIE · CCC code: 0277-786X/11/$18 · doi: 10.1117/12.903360

2.1. Homodyne Photocount Operator

In this subsection we review the quantum description of balanced homodyne detection with a strong coherent-state local oscillator (LO) in an arbitrary spatiotemporal mode. A detailed treatment of homodyne detection with a continuous-wave LO from both the semiclassical and quantum viewpoints may be found in [3, 4]. The relatively minor modification that is needed for the pulsed case is given below.

For a $\sqrt{\text{photons m}^{-2}\text{s}^{-1}}$-units detector plane space-time field operator $\hat{E}(\boldsymbol{\rho}, t)$ being balanced-homodyne detected against the LO coherent-state waveform $\mathcal{E}_{\mathsf{LO}}(\boldsymbol{\rho}, t)$ using detectors with quantum efficiency η, the total photocount operator $\hat{N}^*$ is well approximated by

$$\hat{N} = 2\eta \int_{\mathcal{A}_d \times \mathcal{T}_I} d\boldsymbol{\rho}\, dt\ \mathrm{Re}[\hat{E}(\boldsymbol{\rho}, t)\mathcal{E}^*_{\mathsf{LO}}(\boldsymbol{\rho}, t)] + 2\sqrt{\eta(1-\eta)} \int_{\mathcal{A}_d \times \mathcal{T}_I} d\boldsymbol{\rho}\, dt\ \mathrm{Re}[\hat{E}_\eta(\boldsymbol{\rho}, t)\mathcal{E}^*_{\mathsf{LO}}(\boldsymbol{\rho}, t)], \tag{1}$$

where $\boldsymbol{\rho}$ denotes the transverse spatial coordinate in the the detector plane, and $\hat{E}_\eta(\boldsymbol{\rho}, t)$ is a fictitious field operator in the vacuum state that accounts for the sub-unity quantum efficiency of the detectors. The LO waveform, defined on the product of the detection area $\mathcal{A}_d$ and time interval $\mathcal{T}_I = [0, T_I]$ is given by

$$\mathcal{E}_{\mathsf{LO}}(\boldsymbol{\rho}, t) = \sqrt{n_T N_{\mathsf{LO}}}\, \chi_{\mathsf{LO}}(\boldsymbol{\rho})\, \xi_T(t), \tag{2}$$

where N_{LO} is the average photon number in each LO pulse, $\chi_{\mathsf{LO}}(\boldsymbol{\rho})$ is the normalized LO spatial pattern satisfying

$$\int_{\mathcal{A}_d} |\chi_{\mathsf{LO}}(\boldsymbol{\rho})|^2 d\boldsymbol{\rho} = 1, \tag{3}$$

and $\xi_T(t)$ is the normalized LO temporal pattern obeying

$$\int_{\mathcal{T}_I} |\xi_T(t)|^2 dt = 1. \tag{4}$$

The temporal mode function $\xi_T(t)$ that we will be considering in this paper consists of a train of unit square-integral flat-top pulses $p(t)$:

$$p(t) = \begin{cases} 1/\sqrt{\tau}, & \text{for } 0 \le t \le \tau \\ 0, & \text{otherwise} \end{cases} \tag{5}$$

The period of the pulse train is denoted T (see Fig. 1), so that

$$\xi_T(t) = \frac{1}{\sqrt{n_T}} \left(\sum_{m=0}^{\infty} p(t - mT) \right), \quad t \in \mathcal{T}_I. \tag{6}$$

As the notation suggests, n_T may be thought of as the number of pulses in the integration interval $\mathcal{T}_I$, viz.,

$$n_T = \sum_{m=0}^{\infty} \int_{\mathcal{T}_I} dt\ p^2(t - mT). \tag{7}$$

Note that n_T need not be a whole number. However, the values of τ in the Harris Corp. GCSD experiments [5] are $\sim$200 psec while the integration time in their system is $T_I \sim 1\,\mu$sec, owing to the slow photodetectors employed. Therefore, the edge effects of pulses being cut off by the integration interval are negligible.

The integrands of (1), taken together, are a good approximation for the actual photocount-rate operator when $|\mathcal{E}_{\mathsf{LO}}(\boldsymbol{\rho}, t)|^2 \gg \langle \hat{E}^\dagger(\boldsymbol{\rho}, t)\hat{E}(\boldsymbol{\rho}, t)\rangle$ [3, 4]. For $N_{\mathsf{LO}} \gg 1$, this condition holds at those times when the LO pulse is on. However, for the intervals in which the LO is off, the field $\hat{E}(\boldsymbol{\rho}, t)$ contributes photocounts that are not accounted for in (1). Nevertheless, the integrated photocount over these intervals can be shown to be much less than that from the LO-on intervals for sufficiently high N_{LO} values.

*The operator $\hat{N}$ is the difference of the photocount operators $\hat{N}_1$ and $\hat{N}_2$ at the two detectors.

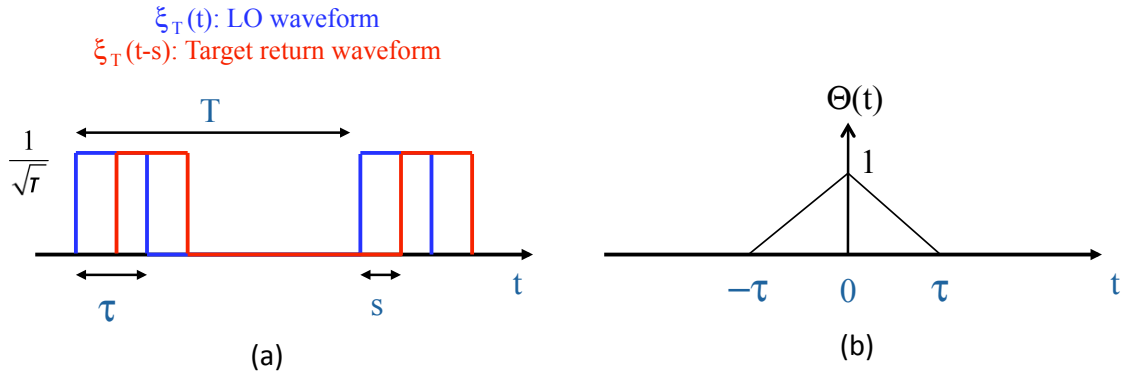

Figure 1. (a) The normalized LO waveform having the shape of the pulse train $\xi_T(t)$ of period T is shown, along with the normalized target-return waveform of shape $\xi_T(t-s)$, where s the roundtrip propagation delay. The pulse width is τ. (b) The overlap integral $\theta(t)$ between pair of pulses (see Eq. (30)).

For a given LO temporal pattern, we may integrate out the time variable in (1) by defining

$$\hat{E}(\boldsymbol{\rho}) = \int_{\mathcal{T}_I} dt\, \hat{E}(\boldsymbol{\rho}, t)\xi_T^*(t) \tag{8}$$

as the purely space-dependent field operator that is in the same time mode as the LO, and use

$$\mathcal{E}_{\mathsf{LO}}(\boldsymbol{\rho}) = \sqrt{n_T N_{\mathsf{LO}}}\,\chi(\boldsymbol{\rho}), \tag{9}$$

to reduce (1) to

$$\hat{N}_T = 2\eta \int_{\mathcal{A}_d} d\boldsymbol{\rho}\ \mathrm{Re}[\hat{E}(\boldsymbol{\rho})\mathcal{E}_{\mathsf{LO}}^*(\boldsymbol{\rho})] + \sqrt{\eta(1-\eta)n_T N_{\mathsf{LO}}}\ (\hat{v} + \hat{v}^\dagger), \tag{10}$$

where $\hat{v}$ is a single-mode annihilation operator in the vacuum state representing the vacuum noise from $\hat{E}_\eta(\boldsymbol{\rho}, t)$. We have labeled the photocount operator with the period T of its LO temporal waveform to allow for multiple measurements at different values of T as required for ranging (see Sect. 4). We have not included detector dark noise in our derivation because, in practice, it is negligible in comparison to the LO shot noise of the baseline system, and even less significant in quantum-enhanced operation.

2.2. Quantum-enhanced Ladar System

The optical setup of the coherent ladar system under consideration is shown in Fig. 2. The input pupil-plane transverse spatial coordinate is denoted $\boldsymbol{\rho}'$ and the field operator in this plane corresponding to the target return is denoted $\hat{E}_R(\boldsymbol{\rho}', t)$. In the following, we will assume the general case of an aperture with a real-valued transmissivity $A(\boldsymbol{\rho}')$ that is hard limited to a disk of diameter D. A typical functional form of a soft aperture transmissivity function is the Gaussian shape:

$$A(\boldsymbol{\rho}') = \begin{cases} \exp\left(-2|\boldsymbol{\rho}'|^2/R^2\right), & \text{for } |\boldsymbol{\rho}'| \le D/2 \\ 0, & |\boldsymbol{\rho}'| \ge D/2. \end{cases} \tag{11}$$

A detector-plane field operator $\hat{E}_{\mathrm{SVI}}^{\mathrm{in}}(\boldsymbol{\rho}, t)$ in its vacuum state enters a squeezer that produces the squeezed output field $\hat{E}_{\mathrm{SVI}}^{\mathrm{out}}(\boldsymbol{\rho}, t)$ (not shown in Fig. 2) that propagates toward the target to become the pupil-plane field operator $\hat{E}_S(\boldsymbol{\rho}', t)$, which mixes with the target-return field $\hat{E}_R(\boldsymbol{\rho}', t)$ according to

$$\hat{E}_R'(\boldsymbol{\rho}', t) = A(\boldsymbol{\rho}')\,\hat{E}_R(\boldsymbol{\rho}', t) + \sqrt{1 - A^2(\boldsymbol{\rho}')}\ \hat{E}_S(\boldsymbol{\rho}', t). \tag{12}$$

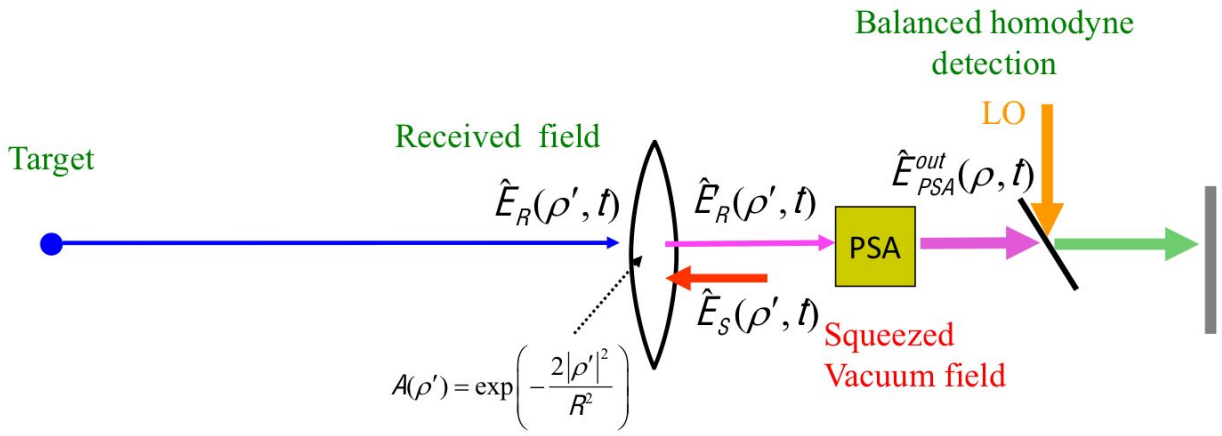

Figure 2. Schematic of optical configuration of a quantum-enhanced homodyne ladar system. $\boldsymbol{\rho}$ and $\boldsymbol{\rho}'$ are respectively detector-plane and pupil-plane transverse coordinates. The output $\hat{E}^{\rm out}_{\rm PSA}(\boldsymbol{\rho},t)$ of a detector-plane phase-sensitive amplifier (PSA) is measured using balanced homodyne detection. If a soft aperture of real-valued transmissivity $A(\boldsymbol{\rho}')$ is used (as pictured), a backward-propagating squeezed vacuum field $\hat{E}_S(\boldsymbol{\rho}',t)$ may be mixed with the target-return field $\hat{E}_R(\boldsymbol{\rho}',t)$ in the pupil plane.

The field operator $\hat{E}'_R(\boldsymbol{\rho}',t)$ subsequently propagates in free space to the image plane to become $\hat{E}^{\rm in}_{\rm PSA}(\boldsymbol{\rho},t)$, which is the input to a phase-sensitive amplifier. The PSA output $\hat{E}^{\rm out}_{\rm PSA}(\boldsymbol{\rho},t)$ is measured using balanced homodyne detection with the LO given by (2).

In the architecture conceived for the Harris experiments [5], the LO temporal waveform $\xi_T(t)$ is the same as the PSA pump waveform and the SVI pump waveform is advanced by the roundtrip time delay, 2Δ, between the detector and pupil planes. Similar to Subsec. 2.1, we may define

$$\hat{E}^{\rm in(out)}_{\rm PSA}(\boldsymbol{\rho}) = \int_{\mathcal{T}_T} dt\, \hat{E}^{\rm in(out)}_{\rm PSA}(\boldsymbol{\rho},t)\xi^*_T(t), \tag{13}$$

$$\hat{E}_R(\boldsymbol{\rho}') = \int_{\mathcal{T}_I} dt\, \hat{E}_R(\boldsymbol{\rho}',t)\xi^*_T(t+\Delta), \tag{14}$$

and

$$\hat{E}^{\rm in(out)}_{\rm SVI}(\boldsymbol{\rho}) = \int_{\mathcal{T}_T} dt\, \hat{E}^{\rm in(out)}_{\rm SVI}(\boldsymbol{\rho},t)\xi^*_T(t+2\Delta). \tag{15}$$

With these definitions, the input-output relations of the squeezer may be written in terms of the purely space-dependent operators as follows:

$$\hat{E}^{\rm out}_{\rm SVI}(\boldsymbol{\rho}) = \int \left[\alpha(\boldsymbol{\rho},\boldsymbol{\rho}')\hat{E}^{\rm in}_{\rm SVI}(\boldsymbol{\rho}') - \beta(\boldsymbol{\rho},\boldsymbol{\rho}')\hat{E}^{\rm in\dagger}_{\rm SVI}(\boldsymbol{\rho}')\right] d\boldsymbol{\rho}', \tag{16}$$

where

$$\alpha(\boldsymbol{\rho},\boldsymbol{\rho}') = \sum_n \sqrt{g'_n}\,\psi_n(\boldsymbol{\rho})\Psi^*_n(\boldsymbol{\rho}') \tag{17}$$

$$\beta(\boldsymbol{\rho},\boldsymbol{\rho}') = \sum_n \sqrt{g'_n - 1}\,\psi_n(\boldsymbol{\rho})\Psi_n(\boldsymbol{\rho}'), \tag{18}$$

for complete orthonormal (CON) sets of spatial mode functions $\{\psi_n\}$ and $\{\Psi_n\}$ on the detector plane and real-valued gain coefficients $\{g'_n \geq 1\}$. These functions describe the spatial-mode characteristics of a real squeezer, as elaborated in [2]. Similar input-output relations hold for the PSA, namely

$$\hat{E}^{\rm out}_{\rm PSA}(\boldsymbol{\rho}) = \int \left[\mu(\boldsymbol{\rho},\boldsymbol{\rho}')\hat{E}^{\rm in}_{\rm PSA}(\boldsymbol{\rho}') + \nu(\boldsymbol{\rho},\boldsymbol{\rho}')\hat{E}^{\rm in\dagger}_{\rm PSA}(\boldsymbol{\rho}')\right] d\boldsymbol{\rho}', \tag{19}$$

where

$$\mu(\boldsymbol{\rho},\boldsymbol{\rho}') = \sum_n \sqrt{g_n}\,\phi_n(\boldsymbol{\rho})\Phi_n^*(\boldsymbol{\rho}') \tag{20}$$

$$\nu(\boldsymbol{\rho},\boldsymbol{\rho}') = \sum_n \sqrt{g_n - 1}\,\phi_n(\boldsymbol{\rho})\Phi_n(\boldsymbol{\rho}'), \tag{21}$$

for CON mode sets $\{\phi_n\}$ and $\{\Phi_n\}$ and gain coefficients $\{g_n \geq 1\}$ (see [2] for details). Using the relations (16) and (19) along with the Fresnel formulas for free-space diffraction between the pupil and detector planes, we can show that the PSA output-field operator may be written in terms of just the target-return field and SVI input-field operators and their adjoints, i.e.,

$$\hat{E}^{\text{out}}_{\text{PSA}}(\boldsymbol{\rho}) = \int d\boldsymbol{\rho}'\big[A_1(\boldsymbol{\rho},\boldsymbol{\rho}')\hat{E}_R(\boldsymbol{\rho}') + A_2(\boldsymbol{\rho},\boldsymbol{\rho}')\hat{E}_R^\dagger(\boldsymbol{\rho}')\big] + \int d\boldsymbol{\omega}\big[B_1(\boldsymbol{\rho},\boldsymbol{\omega})\hat{E}^{\text{in}}_{\text{SVI}}(\boldsymbol{\omega}) + B_2(\boldsymbol{\rho},\boldsymbol{\omega})\hat{E}^{\text{in}\dagger}_{\text{SVI}}(\boldsymbol{\omega})\big], \tag{22}$$

where the four transformation kernels appearing above are given by

$$A_1(\boldsymbol{\rho},\boldsymbol{\rho}') = \int d\boldsymbol{\sigma}\,\frac{A(\boldsymbol{\rho}')}{\lambda d}e^{-ik\boldsymbol{\sigma}\cdot\boldsymbol{\rho}'/d}\mu(\boldsymbol{\rho},\boldsymbol{\sigma}), \tag{23}$$

$$A_2(\boldsymbol{\rho},\boldsymbol{\rho}') = \int d\boldsymbol{\sigma}\,\frac{A(\boldsymbol{\rho}')}{\lambda d}e^{ik\boldsymbol{\sigma}\cdot\boldsymbol{\rho}'/d}\nu(\boldsymbol{\rho},\boldsymbol{\sigma}), \tag{24}$$

$$\begin{aligned} B_1(\boldsymbol{\rho},\boldsymbol{\omega}) = {}& \frac{1}{(\lambda d)^2}\int d\boldsymbol{\sigma}\,d\boldsymbol{\rho}'\,d\boldsymbol{\tau}\,\alpha(\boldsymbol{\tau},\boldsymbol{\omega})e^{-ik\boldsymbol{\rho}'\cdot\boldsymbol{\tau}/d}\sqrt{1-A^2(\boldsymbol{\rho}')}\,e^{-ik\boldsymbol{\sigma}\cdot\boldsymbol{\rho}'/d}\mu(\boldsymbol{\rho},\boldsymbol{\sigma}) \\ & -\frac{1}{(\lambda d)^2}\int d\boldsymbol{\sigma}\,d\boldsymbol{\rho}'\,d\boldsymbol{\tau}\,\beta^*(\boldsymbol{\tau},\boldsymbol{\omega})e^{ik\boldsymbol{\rho}'\cdot\boldsymbol{\tau}/d}\sqrt{1-A^2(\boldsymbol{\rho}')}\,e^{ik\boldsymbol{\sigma}\cdot\boldsymbol{\rho}'/d}\nu(\boldsymbol{\rho},\boldsymbol{\sigma}), \end{aligned} \tag{25}$$

and

$$\begin{aligned} B_2(\boldsymbol{\rho},\boldsymbol{\omega}) = {}& -\frac{1}{(\lambda d)^2}\int d\boldsymbol{\sigma}\,d\boldsymbol{\rho}'\,d\boldsymbol{\tau}\,\beta(\boldsymbol{\tau},\boldsymbol{\omega})e^{-ik\boldsymbol{\rho}'\cdot\boldsymbol{\tau}/d}\sqrt{1-A^2(\boldsymbol{\rho}')}\,e^{-ik\boldsymbol{\sigma}\cdot\boldsymbol{\rho}'/d}\mu(\boldsymbol{\rho},\boldsymbol{\sigma}) \\ & +\frac{1}{(\lambda d)^2}\int d\boldsymbol{\sigma}\,d\boldsymbol{\rho}'\,d\boldsymbol{\tau}\,\alpha^*(\boldsymbol{\tau},\boldsymbol{\omega})e^{ik\boldsymbol{\rho}'\cdot\boldsymbol{\tau}/d}\sqrt{1-A^2(\boldsymbol{\rho}')}\,e^{ik\boldsymbol{\sigma}\cdot\boldsymbol{\rho}'/d}\nu(\boldsymbol{\rho},\boldsymbol{\sigma}). \end{aligned} \tag{26}$$

Here, d is the separation between the pupil and image planes, and $k = 2\pi/\lambda$ is the wavenumber at the ladar wavelength λ. In computing the factors coming from field propagation, we have assumed for simplicity that all global phase factors and the phase curvature at the input to the phase-sensitive amplifier resulting from propagation from the pupil plane to the image plane have been compensated.

Because $\hat{E}^{\text{out}}_{\text{PSA}}(\boldsymbol{\rho})$ is the field operator being detected using homodyne detection, the expression (10) applies with $\hat{E}(\boldsymbol{\rho})$ replaced by $\hat{E}^{\text{out}}_{\text{PSA}}(\boldsymbol{\rho})$:

$$\hat{N}_T = 2\eta\int_{\mathcal{A}_d} d\boldsymbol{\rho}\,\text{Re}[\hat{E}^{\text{out}}_{\text{PSA}}(\boldsymbol{\rho})\mathcal{E}^*_{\text{LO}}(\boldsymbol{\rho})] + \sqrt{\eta(1-\eta)n_T N_{\text{LO}}}\,(\hat{v}+\hat{v}^\dagger). \tag{27}$$

In order to calculate any desired statistics, all that remains to be specified is the quantum state of the input field modes $\hat{E}_R(\boldsymbol{\rho}')$ and $\hat{E}^{\text{in}}_{\text{SVI}}(\boldsymbol{\rho})$ and the mode $\hat{v}$ of (10). *Conditioned on a particular value of the target speckle reflection coefficient*[†], we can describe the state of the system as a joint coherent state $|\psi\rangle$ such that

$$\hat{E}_R(\boldsymbol{\rho}')|\psi\rangle = \mathcal{E}_R(\boldsymbol{\rho}')|\psi\rangle, \tag{28a}$$

$$\hat{E}^{\text{in}}_{\text{SVI}}(\boldsymbol{\rho})|\psi\rangle = 0, \tag{28b}$$

$$\hat{v}|\psi\rangle = 0. \tag{28c}$$

[†]In the case of a specular target, no conditioning in necessary as the reflection coefficient is deterministic.

In other words, the input to the squeezer is in the vacuum state while the target-return field's eigenfunction $\mathcal{E}_R(\rho')$ is given by

$$\mathcal{E}_R(\rho') = r\,\sqrt{N_S}\,\chi(\boldsymbol{\rho}')\int_{\mathcal{T}_I} dt\,\left(\sum_{m=0}^{\infty} p(t-mT-s)\right)\xi_T^*(t) = r\sqrt{n_T N_S}\;\chi(\boldsymbol{\rho}')\theta(s-T). \tag{29}$$

In this expression: $s = 2L/c$ is the roundtrip delay time for a target at range L m from the detector plane, N_S is the average number of signal photons per transmitted pulse (the transmitted pulse train is in a coherent state); r is the roundtrip conditional specular reflection coefficient; and $\chi(\boldsymbol{\rho}')$ is the normalized pupil-plane field pattern produced by the target. Also, $\theta(t)$ is the overlap function between flat-top pulses separated in time by t (see Fig. 1),

$$\theta(t) = \int du\, p(u)p(u-t) = \begin{cases} 1-|t|/\tau, & \text{for } -\tau \le t \le \tau \\ 0, & \text{otherwise,} \end{cases}, \tag{30}$$

so that

$$\int_{\mathcal{T}_I} dt\,\left(\sum_{m=0}^{\infty} p(t-mT-s)\right)\left(\sum_{m'=0}^{\infty} p(t-m'T)\right) = \tag{31}$$

$$\int_{\mathcal{T}_I} dt\,\left(\sum_{m=0}^{\infty} p(t-mT-s)p(t-mT)\right) \cong n_T\,\theta(s-T), \tag{32}$$

neglecting edge effects.

3. RANGING PHOTOCOUNT STATISTICS

We first derive the statistics of the homodyne photocount operator $\hat{N}_T$ of (27) conditioned on the value of the reflectivity r. In Subsect. 3.2, we consider the general case of a target with both specular and speckle reflectivity components.

3.1. Statistics conditioned on target reflectivity

For a given r, and a particular target delay s, we can use (22) and (28) in (27) to show that the characteristic function of the random variable N_T corresponding to the measurement outcome of the operator $\hat{N}_T$ has a Gaussian form. As such, N_T is fully characterized by its mean μ_T and its variance σ_T^2. The mean is given by

$$\mu_T = 2\eta n_T\sqrt{N_{\mathsf{LO}}N_S}\,\mathrm{Re}\left\{r\int d\boldsymbol{\rho}'d\boldsymbol{\rho}\;\chi(\boldsymbol{\rho}')\left[A_1(\boldsymbol{\rho},\boldsymbol{\rho}')\chi_{\mathsf{LO}}^*(\boldsymbol{\rho}) + A_2^*(\boldsymbol{\rho},\boldsymbol{\rho}')\chi_{\mathsf{LO}}(\boldsymbol{\rho})\right]\right\}\theta(s-T). \tag{33}$$

Even in this general form, the following features of μ_T may be discerned:

1. The mean is independent of the parameters of the squeezed-vacuum injection.
2. The mean's dependence on s is in the form of the factor $\theta(s-T)$.

The variance of N_T is found to be

$$\begin{aligned}\sigma_T^2 \;=\;& \eta^2 n_T N_{\mathsf{LO}}\left\{\int d\boldsymbol{\rho}'\left|\int d\boldsymbol{\rho}\,\left[A_1(\boldsymbol{\rho},\boldsymbol{\rho}')\chi_{\mathsf{LO}}^*(\boldsymbol{\rho}) + A_2^*(\boldsymbol{\rho},\boldsymbol{\rho}')\chi_{\mathsf{LO}}(\boldsymbol{\rho})\right]\right|^2\right\} \\ &+\eta^2 n_T N_{\mathsf{LO}}\left\{\int d\boldsymbol{\omega}\left|\int d\boldsymbol{\rho}\,\left[B_1(\boldsymbol{\rho},\boldsymbol{\omega})\chi_{\mathsf{LO}}^*(\boldsymbol{\rho}) + B_2^*(\boldsymbol{\rho},\boldsymbol{\omega})\chi_{\mathsf{LO}}(\boldsymbol{\rho})\right]\right|^2\right\} \\ &+\eta(1-\eta)n_T N_{\mathsf{LO}}.\end{aligned} \tag{34}$$

We see that

1. The variance is independent of the signal field parameters, and, in particular, is independent of s.
2. The variance is a sum of terms related to the PSA, SVI, and sub-unity detector quantum efficiency.
3. The variance is proportional to the average number of LO photons, $n_T N_{\mathsf{LO}}$.

3.1.1. Spatially-broadband squeezing and amplification and the classical baseline

Various special cases of the results (33)-(34) are of interest. For the case of spatially-broadband squeezing and amplification considered in [1], we have

$$\alpha(\boldsymbol{\tau},\boldsymbol{\omega}) = \sqrt{g'}\,\delta(\boldsymbol{\tau}-\boldsymbol{\omega}), \tag{35}$$

$$\beta(\boldsymbol{\tau},\boldsymbol{\omega}) = \sqrt{g'-1}\,\delta(\boldsymbol{\tau}-\boldsymbol{\omega}), \tag{36}$$

$$\mu(\boldsymbol{\rho},\boldsymbol{\sigma}) = \sqrt{g}\,\delta(\boldsymbol{\rho}-\boldsymbol{\sigma}), \tag{37}$$

and

$$\nu(\boldsymbol{\rho},\boldsymbol{\sigma}) = \sqrt{g-1}\,\delta(\boldsymbol{\tau}-\boldsymbol{\omega}). \tag{38}$$

Taking $g = g' = 1$ reduces this spatially-broadband special case to the classical baseline, in which there is no SVI or PSA quantum enhancements.

The preceding expressions for the spatially-broadband case lead to

$$A_1(\boldsymbol{\rho},\boldsymbol{\rho}') = \sqrt{g}A(\boldsymbol{\rho},\boldsymbol{\rho}'), \tag{39}$$

and

$$A_2(\boldsymbol{\rho},\boldsymbol{\rho}') = \sqrt{g-1}\,A(\boldsymbol{\rho},\boldsymbol{\rho}'), \tag{40}$$

where

$$A(\boldsymbol{\rho},\boldsymbol{\rho}') = \frac{A(\boldsymbol{\rho}')}{\lambda d}\,e^{-ik\boldsymbol{\rho}\cdot\boldsymbol{\rho}'/d}. \tag{41}$$

They also give

$$B_1(\boldsymbol{\rho},\boldsymbol{\omega}) = \sqrt{gg'}\,B(\boldsymbol{\rho},\boldsymbol{\omega}) - \sqrt{(g-1)(g'-1)}\,B^*(\boldsymbol{\rho},\boldsymbol{\omega}), \tag{42}$$

and

$$B_2(\boldsymbol{\rho},\boldsymbol{\omega}) = -\sqrt{g(g'-1)}\,B(\boldsymbol{\rho},\boldsymbol{\omega}) + \sqrt{(g-1)(g')}\,B^*(\boldsymbol{\rho},\boldsymbol{\omega}), \tag{43}$$

where

$$B(\boldsymbol{\rho},\boldsymbol{\omega}) = \frac{1}{(\lambda d)^2}\int d\boldsymbol{\rho}'\; e^{-ik(\boldsymbol{\rho}+\boldsymbol{\omega})\cdot\boldsymbol{\rho}'/d}\sqrt{1-A^2(\boldsymbol{\rho}')}. \tag{44}$$

It turns out to be convenient to define the image-plane function

$$\chi_g(\boldsymbol{\rho}) = \sqrt{g}\,\chi_{\mathsf{LO}}(\boldsymbol{\rho}) + \sqrt{g-1}\,\chi^*_{\mathsf{LO}}(\boldsymbol{\rho}), \tag{45}$$

with which notation the mean μ_T, for the spatially-broadband case, is found to be

$$\mu_T = 2\eta n_T\sqrt{N_{\mathsf{LO}}N_S}\,\mathrm{Re}\biggl\{r\int d\boldsymbol{\rho}\biggl[\int d\boldsymbol{\rho}'\;\chi(\boldsymbol{\rho}')A(\boldsymbol{\rho},\boldsymbol{\rho}')\biggr]\chi^*_g(\boldsymbol{\rho})\biggr\}\,\theta(s-T) \tag{46}$$

$$= 2\eta n_T\sqrt{N_{\mathsf{LO}}N_S}\,\mathrm{Re}\biggl\{r\int d\boldsymbol{\rho}\,\mathcal{F}_A[\chi](\boldsymbol{\rho})\chi^*_g(\boldsymbol{\rho})\biggr\}\,\theta(s-T), \tag{47}$$

where we see from the definition of $A(\boldsymbol{\rho},\boldsymbol{\rho}')$ that $\mathcal{F}_A[\chi](\boldsymbol{\rho})$ is exactly $\chi(\boldsymbol{\rho}')$ propagated from the pupil plane through the soft aperture and to the image plane. Hence the second line contains the overlap integral between the image-plane target return and $\chi_g(\boldsymbol{\rho})$. In particular, for the baseline case of $g = 1$, we have $\chi_g(\boldsymbol{\rho}) = \chi_{\mathsf{LO}}(\boldsymbol{\rho})$, so that the integral is the overlap between the target-return mode and the LO mode on the detector plane.

Similarly, the variance σ_T^2 for the spatially-broadband case is found to be

$$\begin{aligned}\sigma_T^2 = {}& \eta^2 n_T N_{\mathsf{LO}}\int d\boldsymbol{\rho}'\biggl|\mathcal{B}_A[\chi^*_g](\boldsymbol{\rho}')\biggr|^2\\ &+\eta^2 n_T N_{\mathsf{LO}}\int d\boldsymbol{\omega}\biggl|\int d\boldsymbol{\rho}\bigl[\sqrt{g'}\,B(\boldsymbol{\rho},\boldsymbol{\omega}) - \sqrt{g'-1}\,B^*(\boldsymbol{\rho},\boldsymbol{\omega})\bigr]\chi^*_g(\boldsymbol{\rho})\biggr|^2\\ &+\eta(1-\eta)n_T N_{\mathsf{LO}},\end{aligned} \tag{48}$$

where $\mathcal{B}_A[\chi_g^*](\boldsymbol{\rho}')$ is the pupil-plane field resulting from propagating $\chi_g^*(\boldsymbol{\rho})$ backwards from the image plane and through the soft aperture, i.e.,

$$\mathcal{B}_A[\chi_g^*](\boldsymbol{\rho}') = \int d\boldsymbol{\rho}\; A(\boldsymbol{\rho},\boldsymbol{\rho}')\chi_g^*(\boldsymbol{\rho}). \tag{49}$$

Examining (44) shows that $B(\boldsymbol{\rho},\boldsymbol{\omega})$ is the kernel for propagation of $\chi_g^*(\boldsymbol{\rho})$ from the image to the pupil plane followed by reflection at the soft aperture and propagation back to the image plane. In the case of no SVI, i.e., $g' = 1$, we see that the integral in the second term of our σ_T^2 formula is the integrated squared-magnitude in this returned waveform, which by the unitarity of propagation is equal to the integrated squared-magnitude just after reflection at the soft aperture. When added to the integral in the first term, the result is the integrated squared-magnitude of $\chi_g(\boldsymbol{\rho})$, so that

$$\sigma_T^2[\text{no SVI}] = \eta^2 n_T N_{\mathsf{LO}} \int d\boldsymbol{\rho} \big|\chi_g(\boldsymbol{\rho})\big|^2 + \eta(1-\eta) n_T N_{\mathsf{LO}}. \tag{50}$$

For baseline operation, $\chi_g(\boldsymbol{\rho}) = \chi_{\mathsf{LO}}(\boldsymbol{\rho})$ has unit integrated squared-magnitude, and the classical homodyne-detection variance is recovered:

$$\sigma_T^2[\text{baseline}] = \eta \mathrm{n_T N_{LO}}. \tag{51}$$

3.1.2. PSA only (no SVI)

When PSA is the only quantum enhancement that is employed, the input field to the amplifier, $\hat{E}^{\text{in}}_{\text{PSA}}(\boldsymbol{\rho})$, is in a coherent state with eigenfunction

$$\mathcal{E}_{\text{PSA}}(\boldsymbol{\sigma}) = r\sqrt{n_T N_S}\, \mathcal{F}_A[\chi](\boldsymbol{\sigma})\theta(s-T). \tag{52}$$

We then have from

$$\hat{E}^{\text{out}}_{\text{PSA}}(\boldsymbol{\rho}) = \int d\boldsymbol{\sigma}\; \hat{E}^{\text{in}}_{\text{PSA}}(\boldsymbol{\sigma})\mu(\boldsymbol{\rho},\boldsymbol{\sigma}) + \int d\boldsymbol{\sigma}\; \hat{E}^{\text{in}}_{\text{PSA}}(\boldsymbol{\sigma})^\dagger \nu(\boldsymbol{\rho},\boldsymbol{\sigma}), \tag{53}$$

that

$$\begin{aligned}\hat{N}_T \;=\; & \eta\sqrt{n_T N_{\mathsf{LO}}}\Big\{ \int d\boldsymbol{\rho}\, d\boldsymbol{\sigma}\; \big[\mu(\boldsymbol{\rho},\boldsymbol{\sigma})\chi^*_{\mathsf{LO}}(\boldsymbol{\rho}) + \nu^*(\boldsymbol{\rho},\boldsymbol{\sigma})\chi_{\mathsf{LO}}(\boldsymbol{\rho})\big]\hat{E}_R(\boldsymbol{\sigma}) \\ & + \int d\boldsymbol{\rho}\, d\boldsymbol{\sigma}\; \big[\mu^*(\boldsymbol{\rho},\boldsymbol{\sigma})\chi_{\mathsf{LO}}(\boldsymbol{\rho}) + \nu(\boldsymbol{\rho},\boldsymbol{\sigma})\chi^*_{\mathsf{LO}}(\boldsymbol{\rho})\big]\hat{E}_R(\boldsymbol{\sigma})^\dagger \Big\} + \sqrt{\eta(1-\eta)n_T N_{\mathsf{LO}}}\; (\hat{v}+\hat{v}^\dagger).\end{aligned} \tag{54}$$

The following expressions for μ_T and σ_T^2 follow from (54):

$$\mu_T = 2\eta n_T \sqrt{N_S N_{\mathsf{LO}}}\; \mathrm{Re}\Big[r \int d\boldsymbol{\sigma}\, d\boldsymbol{\rho}\; \big[\mu^*(\boldsymbol{\rho},\boldsymbol{\sigma})\chi_{\mathsf{LO}}(\boldsymbol{\rho}) + \nu(\boldsymbol{\rho},\boldsymbol{\sigma})\chi^*_{\mathsf{LO}}(\boldsymbol{\rho})\big]\mathcal{F}_A[\chi](\boldsymbol{\sigma})\Big]\theta(s-T), \tag{55}$$

and

$$\sigma_T^2 = \eta^2 n_T N_{\mathsf{LO}} \int d\boldsymbol{\sigma} \left| \int d\boldsymbol{\rho}\; \big[\mu^*(\boldsymbol{\rho},\boldsymbol{\sigma})\chi_{\mathsf{LO}}(\boldsymbol{\rho}) + \nu(\boldsymbol{\rho},\boldsymbol{\sigma})\chi^*_{\mathsf{LO}}(\boldsymbol{\rho})\big] \right|^2 + \eta(1-\eta) n_T N_{\mathsf{LO}}. \tag{56}$$

3.2. Target with mixed reflectivity

We now consider the general case of a target whose reflectivity during the mth pulse of the T-sec-period signal train is given by

$$R_T^{(m)} = \rho + r_T'^{(m)}. \tag{57}$$

Here, ρ is the reflectivity's specular component, which is independent of the pulse number and T value. Each speckle coefficient $r_T'^{(m)}$ is a circular-symmetric, zero-mean, complex-valued Gaussian random variable with quadrature variance $\gamma_T^{(m)}/2 < 1/2$. The total average intensity-reflection coefficient during the mth pulse is therefore $|\rho|^2 + \gamma_T^{(m)}$. Depending on the speckle's temporal behavior, correlations may exist among the different $r_T'^{(m)}$.

Because our slow photodetectors integrate over n_T pulses, the total photocount random variable is

$$N_T = \sum_{m=1}^{n_T} N_T^{(m)}, \tag{58}$$

where $N_T^{(m)}$ is the photocount registered by the mth pulse. Conditioned on $R_T^{(m)}$, the theory of Sect. 3.1 applies to the random variables $N_T^{(m)}$ with $r = R_T^{(m)}$ and the caveat that in the formulas (33), (34) for the means and variances, we set the number of pulses $n_T = 1$.

We will use I to denote the integral

$$I = \int d\boldsymbol{\rho}'\, d\boldsymbol{\rho}\; \chi(\boldsymbol{\rho}')\big[A_1(\boldsymbol{\rho},\boldsymbol{\rho}')\chi_{\mathsf{LO}}^*(\boldsymbol{\rho}) + A_2^*(\boldsymbol{\rho},\boldsymbol{\rho}')\chi_{\mathsf{LO}}(\boldsymbol{\rho})\big] \tag{59}$$

appearing in (33). It is convenient to split each $N_T^{(m)}$ into its specular, speckle, and quantum-noise contributions according to

$$N_T^{(m)} = 2\eta\sqrt{N_{\mathsf{LO}}N_S}\,\theta(s-T)\;\mathrm{Re}(\rho I) + 2\eta\sqrt{N_{\mathsf{LO}}N_S}\,\theta(s-T)\;r_T^{(m)}|I| + Q_T^{(m)}, \tag{60}$$

where $r_T^{(m)}$ is a *real-valued*, zero-mean $\gamma_T^{(m)}/2$-variance Gaussian random variable, and $Q_T^{(m)}$ is the zero-mean Gaussian-distributed quantum noise whose variance is given by (34) with $n_T = 1$. The different $Q_T^{(m)}$ are statistically independent and also independent of the $r_T^{(m)}$.

We now calculate the unconditional statistics of N_T. It is clear that N_T is still a Gaussian random variable, although its variance will differ from (34) unless the target is specular. As we will see in Sect. 4.1, ranging requires that we obtain a set of homodyne photocounts $\{N_T\}$ collected over a sequence of T_I-sec-long measurement intervals as T is stepped from T_{min} to T_{max}. For a target whose reflectivity contains a speckle component, two such photocounts, N_T and $N_{T'}$, may be correlated.

The unconditional mean of N_T for a mixed target is

$$\mu_T = 2\eta n_T\sqrt{N_{\mathsf{LO}}N_S}\,\theta(s-T)\;\mathrm{Re}(\rho I), \tag{61}$$

and is thus a function of the specular reflectivity alone. The unconditional covariance,

$$K_{TT'} = \langle (N_T - \mu_T)(N_{T'} - \mu_{T'})\rangle, \tag{62}$$

between two homodyne photocounts is

$$K_{TT'} = 4\eta^2 N_{\mathsf{LO}}N_S|I|^2\theta(s-T)\;\theta(s-T')\sum_{m=1}^{n_T}\sum_{m'=1}^{n_T'}\langle r_T^{(m)}r_{T'}^{(m')}\rangle + \sigma_T^2\;\delta_{TT'}, \tag{63}$$

where σ_T^2 is given by (34), and $\delta_{TT'}$ is the Kronecker delta function. It is apparent that the covariance depends on the speckle's temporal behavior. The following special cases span the behaviors that might be encountered in real applications:

1. **Fast-varying speckle**: If the target's speckle characteristics change on a time scale faster than T seconds, we may set $\langle r_T^{(m)}r_{T'}^{(m')}\rangle = (\gamma_T^{(m)}/2)\;\delta_{mm'}\delta_{TT'}$ to get

$$K_{TT'} = 2\eta^2 N_{\mathsf{LO}}N_S\Big(\sum_{m=1}^{n_T}\gamma_T^{(m)}\Big)|I|^2\theta^2(s-T)\;\delta_{TT'} + \sigma_T^2\;\delta_{TT'}. \tag{64}$$

2. **Moderately-fast-varying speckle**: If the target's speckle characteristics do not change appreciably within the $n_T T$-sec duration of a single homodyne-photocount measurement, but are independent across the different homodyne-photocount measurements, we have $\langle r_T^{(m)}r_{T'}^{(m')}\rangle \approx (\gamma_T/2)\;\delta_{TT'}$ from which we get

$$K_{TT'} = 2\eta^2 N_{\mathsf{LO}}N_S n_T^2\gamma_T|I|^2\theta^2(s-T)\;\delta_{TT'} + \sigma_T^2\;\delta_{TT'}. \tag{65}$$

3. **Temporally-constant speckle**: If the target reflectivity is unchanged throughout the entire sequence of homodyne-photocount measurements, we have $\langle r_T^{(m)} r_{T'}^{(m')} \rangle = \gamma/2$. For a stationary target and probe beam, this is expected to be the relevant case. The $N_T^{(m)}$ are now correlated across different pulse-repetition periods, with covariance given by

$$K_{TT'} = 2\eta^2 N_{\mathsf{LO}} N_S n_T n_{T'} \gamma |I|^2 \theta(s-T)\ \theta(s-T') + \sigma_T^2\ \delta_{TT'}. \tag{66}$$

4. MAXIMUM-LIKELIHOOD RANGE ESTIMATION AND SIMULATION RESULTS

Suppose that s is known to be in the interval $[s_{\mathsf{min}}, s_{\mathsf{max}}]$. For example, a laboratory-range target that may be 9 -to-15 m away from the ladar will have a range delay that lies in the 60-to-100 ns interval. Further suppose that the pulse-repetition period T is chosen to lie in $[s_{\mathsf{min}} - \tau, s_{\mathsf{max}} + \tau]$, and measurements of N_T are taken at different values of T varying between $T_{\mathsf{min}} = s_{\mathsf{min}} - \tau$ and $T_{\mathsf{max}} = s_{\mathsf{max}} + \tau$. Then it is guaranteed that the $(m+1)$st LO pulse will overlap the mth target-return pulse at some T and moves through it as T is varied from T_{min} to T_{max}. Range estimation then proceeds by measuring homodyne photocounts of the target at a set of K different values of T to obtain a count vector

$$\mathbf{N} = \left[\ N_1 \quad N_2 \quad \cdots \quad N_K\ \right]^T \equiv \left[\ N_{T_1} \quad N_{T_2} \quad \cdots \quad N_{T_K}\ \right]^T \tag{67}$$

followed by the maximum-likelihood processing described below.

4.1. Maximum-likelihood range estimation

The probability density function for $\mathbf{N}$ given the value of s is Gaussian, and fully characterized by the mean vector

$$\boldsymbol{\mu}_s = \left[\ \mu_1 \quad \mu_2 \quad \cdots \quad \mu_K\ \right]^T \equiv \left[\ \mu_{T_1} \quad \mu_{T_2} \quad \cdots \quad \mu_{T_K}\ \right]^T, \tag{68}$$

and the covariance matrix $\tilde{\mathbf{K}}$, whose kk'th element is $K_{kk'} \equiv K_{T_k T_{k'}}$, where the means are given by (61) and the covariances by (63). The probability density function for an observation $\mathbf{N} = \mathbf{n}$, given s, is therefore

$$p(\,\mathbf{n} \mid s\,) = \frac{1}{(2\pi)^{K/2} |\tilde{\mathbf{K}}|^{1/2}}\, e^{-(\mathbf{n}-\boldsymbol{\mu}_s)^T \tilde{\mathbf{K}}^{-1} (\mathbf{n}-\boldsymbol{\mu}_s)/2}, \tag{69}$$

which, as a function of s, is the likelihood function for range estimation. In particular, the maximum-likelihood (ML) range estimate $\hat{s}_{\mathrm{ML}}$ when $\mathbf{N} = \mathbf{n}$ is observed is

$$s_{\mathrm{ML}} = \arg\max_s p(\,\mathbf{n} \mid s\,), \tag{70}$$

and is computed using a numerical-maximization routine.

4.2. Simulation results

We now discuss simulation results corroborating the theory developed above. For simplicity, we will confine ourselves to the most common case of a hard aperture of diameter D, so that

$$A(\boldsymbol{\rho}') = \begin{cases} 1, & \text{for } |\boldsymbol{\rho}'| \le D/2 \\ 0, & |\boldsymbol{\rho}'| \ge D/2. \end{cases} \tag{71}$$

From (12), it is apparent that the field operator $\hat{E}_S(\boldsymbol{\rho}', t)$ which contains the SVI component does not contribute to the post-aperture pupil-plane field operator $\hat{E}_R(\boldsymbol{\rho}', t)$ and hence the measured statistics. It follows that PSA-only operation is sufficient for quantum enhancement of a hard-aperture homodyne ladar. We will consider only the spatially-broadband case of uniform gain coefficients $g_n \equiv g$ from Subsect. 3.1.1, with

$$G_{\mathrm{PSA}} \equiv (\sqrt{g} + \sqrt{g-1})^2. \tag{72}$$

We will, however, consider both the specular and mixed-target cases. In the following, we consider a hard aperture of diameter $D = 2$ mm, operating wavelength $\lambda = 1.5\mu$m, a 1 ns pulse width, and a target at range $L = 1$ km from the detector plane.

We first consider a specular target of effective reflection coefficient $r = 0.5$. We will assume $N_S = 10^3$, $N_{\mathsf{LO}} = 10^6$ for the average number of signal and LO photons per pulse, and take $n_T = 1$ in the integration interval. (Note that increasing n_T scales both the mean and variance by a factor of n_T.) Figure (3a) plots the squared mean and the variance as a function of the detection quantum efficiency η for both the baseline (dashed curves) and PSA-enhanced operation (solid curves) with $G_{\rm PSA} = 11.4\,$dB. Figure (3b) shows the signal-to-noise ratio (SNR) defined as

$$\mathrm{SNR} = \frac{\mu_T^2}{\sigma_T^2} \tag{73}$$

as a function of η. It is evident that PSA provides an SNR improvement when $\eta < 1$ that could potentially improve range resolution.

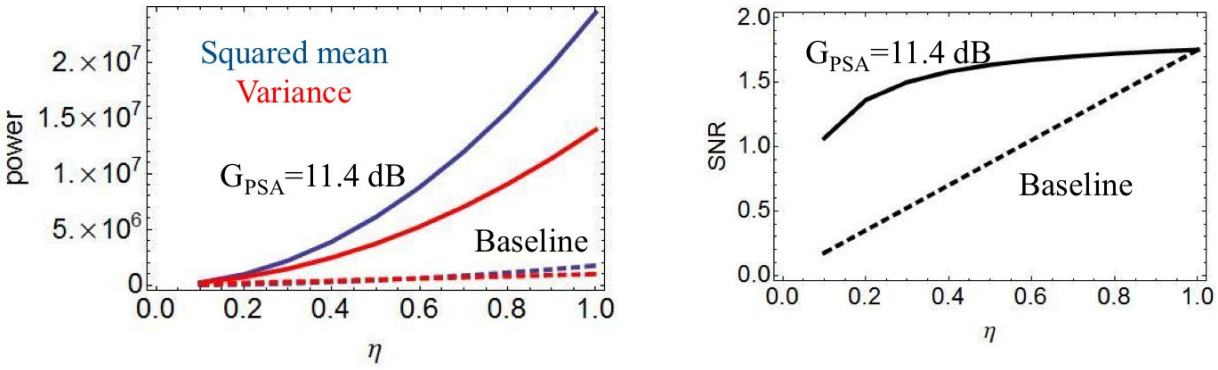

Figure 3. (a) Squared-mean and variance of N_T plotted versus detection efficiency η for baseline and PSA-only operation with $G_{\rm PSA} = 4$, $N_S = 10^3$, $N_{\mathsf{LO}} = 10^6$, and $n_T = 1$. (b) Signal-to-noise ratio (SNR) versus η. PSA improves SNR when $\eta < 1$. Both (a) and (b) are for a specular target with reflectivity $r = 0.5$ at distance $L = 1\,$km. The operating wavelength is $\lambda = 1.5\,\mu$m and the pulse duration is $\tau = 1\,$ns. In both (a) and (b) the solid curves are for PSA-enhanced operation and the dashed curves are for baseline operation.

Figure 4 depicts how the ML range estimate is obtained. It corresponds to baseline operation with the same specular target from Fig. 3. A total of 30 N_T observations were simulated at T values spaced 0.2 ns apart that were centered on the target's range delay s; the points in Fig. 4 are these simulated photocounts. For a specular target, the different N_T are statistically independent so that the likelihood function (69) (plotted as the blue (light) curve) has the simple form specified in the figure. For this data set, the ML range-delay estimate satisfies $s_{\rm ML} - s = -0.1\,$ns; target range is then estimated from $L_{\rm ML} = cs_{\rm ML}/2$ where c is the speed of light.

For the chosen system and target parameters, we made 1000 Monte Carlo runs of the ML estimator, in order to assess the variance of $s_{\rm ML}$. These simulations were repeated for PSA-enhanced situations with various values of $G_{\rm PSA}$. As shown in Fig. 5, the variance of the ML estimate decreases from the baseline case with increasing PSA gain but saturates when $G_{\rm PSA} \gg 1/\eta$. This behavior can be understood qualitatively as follows. According to (50), the photocount variance is the sum of a PSA-gain-dependent term and a detector efficiency term. The mean (47) is, like the variance, a function of the gain through $\chi_g(\boldsymbol{\rho})$ of (45). For high gains, the first term of the variance dominates. However, further increasing the gain has little effect on the SNR, as both the squared mean and the variance increase at the same rate once the detector efficiency noise has been overcome.

Finally, we consider a mixed target example with $\rho = 0.5$ and speckle characteristic $\gamma_T = 0.08$. We assume moderately-fast-varying speckle for the photocount measurements at different T values, so that (65) applies for the covariance matrix $\tilde{\mathbf{K}}$ of the observations. Figure 6 shows the root-mean-square error of the ML range

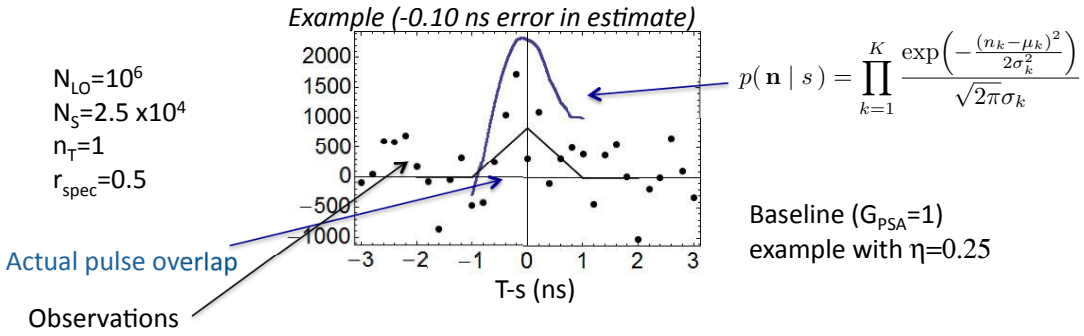

Figure 4. Baseline homodyne-photocount simulations for different T-values, shown as points. The likelihood function, shown as the continuous blue curve, is obtained from these observations. The ML range-delay estimate is the maximum value of this likelihood function. The triangular curve is the pulse overlap function $\theta(T - s)$.

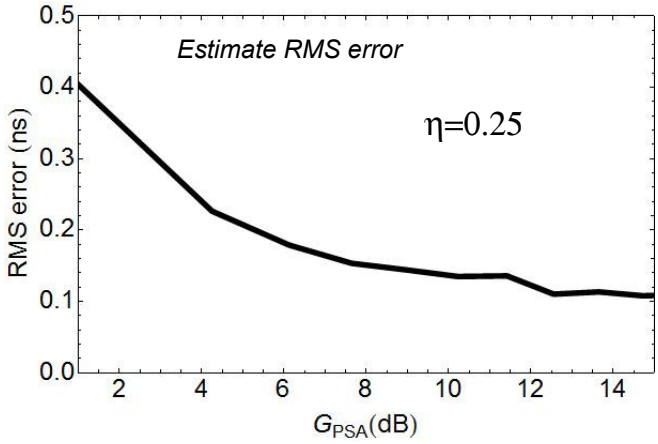

Figure 5. The root-mean-square (RMS) error of the ML estimator s_{ML} as a function of G_{PSA}. The RMS error decreases until $G_{\mathrm{PSA}} \gg 1/\eta$, after which it saturates.

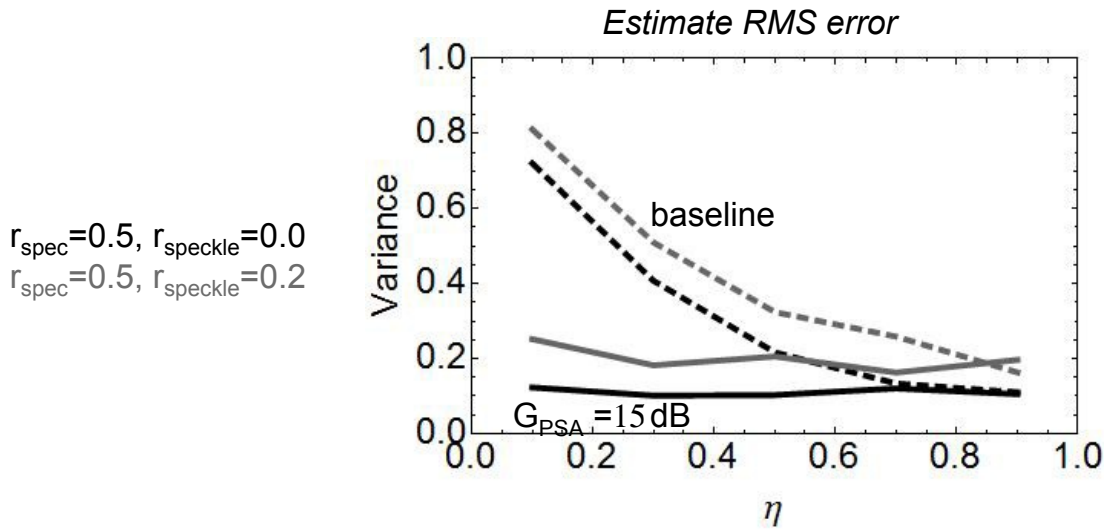

Figure 6. The root-mean-square (RMS) error of the ML estimator s_{ML} as a function of η for a purely specular (black curves) and a mixed (gray curves) target. The mixed-target performance is worse for both baseline and PSA-enhanced operation.

estimator computed using Monte Carlo simulations for both the specular-target case considered earlier, and the mixed-target case. As might have been foretold, the increased uncertainty in reflectivity of the mixed target results in degradation of range-estimation performance for all η values in both the baseline and PSA-enhanced cases. However, the root-mean-square error of the PSA-enhanced case degrades much more gracefully than the baseline case as the detector quantum efficiency decreases from unity.

5. CONCLUSION

We considered the problem of maximum-likelihood range estimation in a homodyne ladar system with or without quantum enhancements from squeezed-vacuum injection (SVI) and phase-sensitive amplification (PSA). For both purely specular and specular-plus-speckle reflectivity targets, general formulas were derived for the Gaussian-distributed photocount statistics for pulsed ladar operation in which ranging is performed by stepping the transmitted and LO pulse periods through a sequence of values and processing the resultant vector of photocounts. The photodetectors were assumed to be slow, so that a large number of pulses are integrated in every photocount observation. Simulation results were presented for the case of a hard aperture with and without spatially-broadband PSA enhancement. In general, the effect of PSA is to mitigate the SNR degradation due to sub-unity detector quantum efficiency. The variance of the range estimate was concomitantly shown to be improved, both in the specular and mixed-target cases, by application of the PSA enhancement. For a given soft-aperture baseline system, the use of SVI in addition to PSA is expected to yield further range-estimation improvement.

ACKNOWLEDGMENTS

This work was supported by the DARPA Quantum Sensor Program, under AFRL Contract No. FA8750-09-C-0194.

REFERENCES

1. Z. Dutton, J. H. Shapiro, and S. Guha, "LADAR resolution improvement using receivers enhanced with squeezed-vacuum injection and phase-sensitive amplification," J. Opt. Soc. Am. B **27,** A63–A72 (2010); Z. Dutton, J. H. Shapiro, and S. Guha, "LADAR resolution improvement using receivers enhanced with squeezed-vacuum injection and phase-sensitive amplification: erratum," J. Opt. Soc. Am. B **27,** 2007–2008 (2010).

2. C. Santivanez, S. Guha, Z. Dutton, M. Annamalai, M. Vasilyev, B. J. Yen, R. Nair, and J. H. Shapiro, "Quantum enhanced LIDAR resolution with multi-spatial-mode phase sensitive amplification," (Paper 8163-34 of SPIE Optics+Photonics 2011).
3. J. H. Shapiro, "Quantum noise and excess noise in optical homodyne and heterodyne receivers," IEEE J. Quantum Electron. **QE-21,** 237–250 (1985).
4. J. H. Shapiro, "The quantum theory of optical communications," IEEE J. Sel. Top. Quantum Electron. **15,** 1547–1569 (2009).
5. P. A. Wasilousky, *et al.*, "Quantum enhancement of a coherent LADAR receiver using phase-sensitive amplification," (Paper 8163-5 of SPIE Optics+Photonics 2011).